# Precipitation Diurnal Cycle over the Maritime Continent Modulated by the Climatological Annual Cycle

JIAHAO LU[a], TIM LI,[b,a] AND LU WANG[a]

[a] *Key Laboratory of Meteorological Disaster, Ministry of Education/Joint International Research Laboratory of Climate and Environmental Change/Collaborative Innovation Center on Forecast and Evaluation of Meteorological Disasters, Nanjing University of Information Science and Technology, Nanjing, China*
[b] *International Pacific Research Center and Department of Atmospheric Sciences, School of Ocean and Earth Science and Technology, University of Hawai'i at Mānoa, Honolulu, Hawaii*

(Manuscript received 26 February 2020, in final form 19 September 2020)

ABSTRACT: The modulation of the diurnal cycle (DC) of precipitation over the Maritime Continent (MC) by the background annual cycle mean state was studied for the period of 1998–2014 through observational analyses and high-resolution simulations using the Weather Research and Forecasting (WRF) Model. The observational analyses reveal that there are statistically significant differences in the DC amplitude between boreal winter and summer. The amplitude of precipitation DC reduces by about 35% during boreal summer compared to boreal winter, especially over the MC major islands and adjacent oceans. A precipitation budget analysis indicates that the DC amplitude difference is primarily attributed to vertically integrated convergence of the mean moisture by diurnal winds. The relative roles of the background dynamic and thermodynamic states in causing the enhanced diurnal wind activity in boreal winter are further investigated through idealized WRF simulations. The results show that the seasonal mean background moisture condition is most critical in inducing the winter–summer difference of the precipitation DC over the MC, followed by atmospheric static stability (i.e., vertical temperature gradient) and circulation conditions.

KEYWORDS: Maritime Continent; Diurnal effects; Precipitation; Moisture/moisture budget; Annual variations

## 1. Introduction

The Maritime Continent (MC) is located in the center of the warm pool connecting the tropical Indian Ocean and western Pacific (Fig. 1). It consists of many islands and shallow oceans with complex land–sea and topography distributions. With abundant moisture, the MC is one of the wettest regions on Earth, with a large annual amount of precipitation. The latent heat release from the precipitation drives the atmospheric circulation throughout the tropics and even affects the middle latitudes (Ramage 1968; Simpson et al. 1993; Neale and Slingo 2003). Therefore, examining the variability of the rainfall over the MC is critical for a better understanding of the regional and global climate.

The rainfall variability in the MC exhibits a wide range of temporal scales from diurnal to interdecadal (Qian 2008; Rauniyar and Walsh 2013). The diurnal cycle is one of the most important components of natural climate variability in the MC region (Yang and Slingo 2001). There has been a long history of research on the diurnal cycle (DC) of precipitation in the tropics using in situ and satellite observations (e.g., Gray and Jacobson 1977; Hendon and Woodberry 1993; Janowiak et al. 1994; Yang and Slingo 2001; Tian et al. 2004; Yang and Smith 2006; Kikuchi and Wang 2008). A marked contrast of DC between the land- and ocean-based cycles was revealed. The primary peak in precipitation tends to occur in the late afternoon or evening over the land, driven by thermal destabilization of the atmosphere from solar radiative heating of the surface during daytime (Yang and Smith 2006), whereas the ocean has a relatively moderate DC with a peak in the early morning. Several mechanisms for the early morning ocean peak have been suggested. They include 1) nighttime radiative cooling at the top of clouds that destabilizes the upper troposphere and raises the height of the tropopause (Kraus 1963; Randall et al. 1991), 2) stronger radiative cooling at night over clear-sky than cloudy regions that enhances low-level convergence into cloudy regions and helps to further organize convection (Gray and Jacobson 1977), 3) greater tropospheric relative humidity and moisture at night (Sui et al. 1997; Frenkel et al. 2011), 4) the life cycle of cloud systems that form in the afternoon and develop into mesoscale convective systems (MCSs) that mature in the early morning (Chen and Houze 1997), and 5) an effect of the semidiurnal tides on the early morning rainfall over ocean (Deser and Smith 1998; Dai 2001). The relative roles of the mechanisms proposed above, however, are unclear so far, and no consensus has been reached (Sakaeda et al. 2017, 2018). Coastal areas often show offshore diurnal propagation of precipitation associated with gravity waves and land–sea breezes (e.g., Dai 2001; Yang and Slingo 2001; Kikuchi and Wang 2008; Love et al. 2011; Biasutti et al. 2012). The MC has many localized effects on the DC in this region (e.g., Mori et al. 2004; Zhou and Wang 2006; Ichikawa and Yasunari 2006, 2008; Wu et al. 2009; Rauniyar and Walsh 2011). The temporal and spatial distributions of precipitation DC are related to the DC of insolation, the land–sea breeze circulation, and the mountain–valley breeze circulation (Chang et al. 2005; Qian et al. 2010).

The MC rainfall exhibits a clear annual cycle, for interactions between the complex terrain and a simple annual reversal of the surface monsoonal winds throughout all monsoon regions from the

*Corresponding author*: Tim Li, timli@hawaii.edu

DOI: 10.1175/JCLI-D-20-0130.1

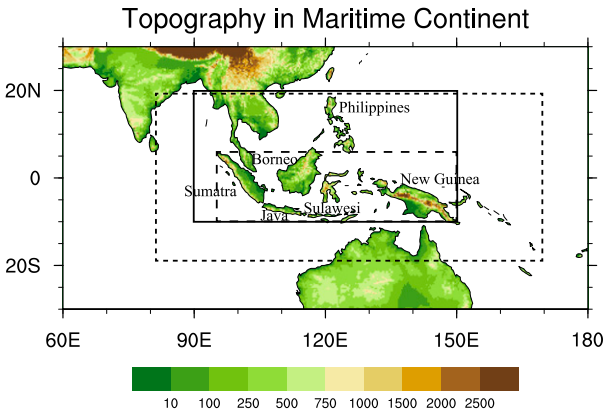


FIG. 1. Topography (m) of the Maritime Continent (MC), with major islands and island groups labeled. The solid black box marks the region of the MC (10°S–20°N, 90°–150°E), the long-dashed black box marks the area of MMC (10°S–6°N, 95°–150°E), and the short-dashed black box marks the model domain.

Indian Ocean to the South China Sea and the equatorial western Pacific (Chang et al. 2005). A wet season occurs during boreal winter (December–February) and a dry season occurs during boreal summer (June–August), under the impact of Asian and Australian monsoons (Ramage 1971). There are significant contrasts in the prevailing wind and water vapor supply between wet and dry seasons, in addition to the seasonal variation of solar radiation. A typical wet (dry) season is accompanied by the monsoon westerlies (easterlies) north of Australia. Following previous studies (e.g., Haylock and McBride 2001; Hendon 2003; Chang et al. 2004; Jiang and Li 2018), in this work we refer to JJA (June–August) as a dry season and DJF (December–February) as a wet season over the MC.

Most of the previous studies on the diurnal variation of precipitation over the MC region have focused on the wet season, during which a large number of rainfall events occur. For example, a number of studies have examined the influence of ENSO and the MJO on the DC of precipitation during boreal winter over the MC and northern Australia (e.g., Qian et al. 2010; Rauniyar and Walsh 2011, 2013; Peatman et al. 2014, 2015; Birch et al. 2016; Sakaeda et al. 2017, 2018; Hung and Sui 2018). Rauniyar and Walsh (2013) suggested that the MC shows localized differences in the modulation of the ENSO phases on the diurnal amplitude of rainfall. Physical explanations for this modulation include the presence of the rising branch of Walker circulation and the link between rainfall anomalies and local moisture convergence. Peatman et al. (2014, 2015) showed that the passage of the MJO modulates the amplitude and phase of the diurnal cycle of rainfall and cloudiness. The amplitude of the precipitation DC tends to peak a few days prior to the arrival of MJO convective centers over the islands of the MC, and the influence of the MJO on the DC amplitude differs between land and ocean. The timing of the peak rainfall tends to be delayed by a few hours within the convectively enhanced envelopes of the MJO, and this delay is due to increased development of stratiform-anvil rainfall following the peak of deep convection (Sakaeda et al. 2017, 2018). There are also scale interactions between the DC and equatorial waves over the MC. Vincent et al. (2016) showed that the DC of precipitation changes with convectively coupled Kelvin and equatorial Rossby waves in a manner similar to that of the MJO. Baranowski et al. (2016) documented that the DC over the islands of the MC can be phase-locked to convectively coupled Kelvin waves.

Although there are fewer rainfall events and less rainfall amount in the dry season, analyzing the DC of precipitation at this time and the seasonality of it is helpful in understanding the physical mechanisms of the precipitation DC over the MC. Several studies have examined the seasonal variation of the DC of precipitation over the region. Sakurai et al. (2005) and As-syakur et al. (2019) investigated the seasonal differences in the diurnal cycle of rainfall and cloud system migration over Sumatra. Their study revealed that the appearance latitude of eastward cloud migration varied seasonally and existed only when the low-level tropospheric wind was westerly, while westward cloud migration appeared over the entire island during virtually all seasons. The propagating characteristics were rather complicated, depending on location and season. Worku et al. (2019) documented that the diurnal variation of rainfall, convection, and precipitation features over the MC have greater amplitude during DJF than JJA. However, in previous studies the analysis of the seasonal change in the diurnal rainfall over the MC has been limited to a particular location such as Sumatra (Sakurai et al. 2005; Yanase et al. 2017; As-syakur et al. 2019) or focused on the migration only. Therefore, it is still worth studying the seasonal variation of the precipitation DC over the MC more comprehensively using data from much-longer periods and covering a wider region.

So far it is not clear through what physical (dynamic or thermodynamic) processes the climatological annual cycle modulates the DC of precipitation over the MC. The objective of the present study is to understand the relative roles of atmospheric moisture, vertical temperature profile, and circulation fields associated with the annual cycle in affecting the precipitation DC over the MC through a series of idealized numerical simulations with the Weather Research and Forecasting (WRF) Model. The remainder of the paper is organized as follows. In section 2, the datasets, analysis methods, and numerical models to be used are described. Section 3 is devoted to presenting general features of the DC during different seasons. Mechanisms responsible for the modulation of climatological annual cycle on DC and the verification by WRF modeling are discussed in section 4. Section 5 gives a brief conclusion and discussion.

## 2. Data, methods, and model formulation

### a. Data

The primary datasets employed in this study include 1) The Tropical Rainfall Measuring Mission (TRMM) 3B42 version 7 data with 3-hourly temporal and 0.25° horizontal resolution (Huffman et al. 2007); 2) the TRMM 3G68 version 7 PR data with hourly temporal and 0.5° horizontal resolution (these data are available online at https://pps.gsfc.nasa.gov); 3) hourly evaporation data from Modern-Era Retrospective Analysis for Research and Applications (MERRA; Rienecker et al. 2011)

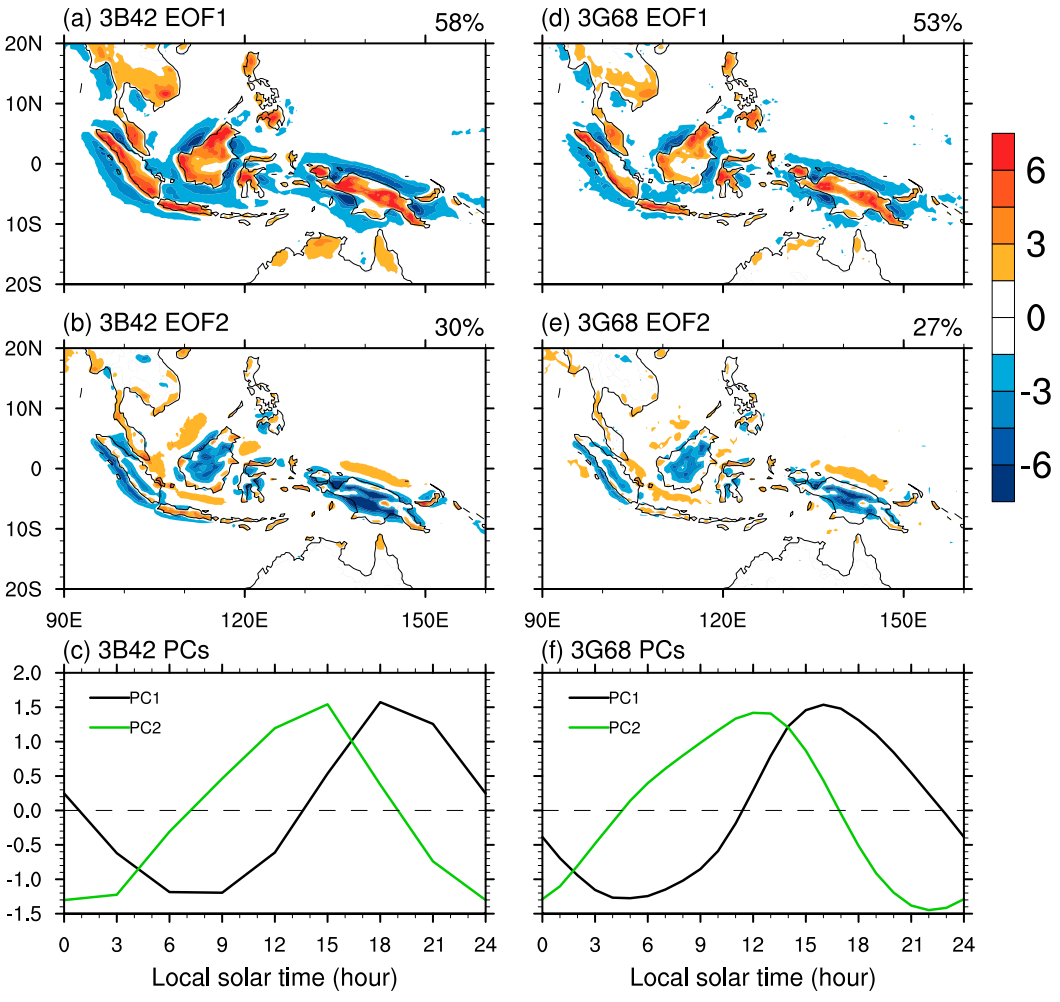


FIG. 2. The leading two EOF modes of precipitation DC averaged from 1998 to 2014: the horizontal distributions of (a),(d) EOF1 and (b),(e) EOF2, and (c),(f) the time series of PC1 and PC2 (mm day$^{-1}$). Results are from (left) TRMM 3B42 and (right) TRMM 3G68.

tavg1_2d_flx_Nx dataset, 3-hourly horizontal wind and specific humidity data from MERRA inst3_3d_asm_Cp dataset; and 4) elevation data from the Earth Topography-2 min (ETOPO2; Smith and Sandwell 1997). The analysis period for all the data spans from 1998 to 2014. The horizontal resolutions of the MERRA product and ETOPO2 used in the study are 1.25° × 1.25° and 2′ of latitude × 2′ of longitude, respectively.

### b. Methods

To focus on the diurnal variation and reduce higher-frequency noises, a 4-h running mean was applied to the original hourly 3G68 data (Negri et al. 2002). An EOF analysis was further applied to obtain the first and second leading modes of the observed precipitation DC, following Lorenz (1956).

A moisture budget analysis was applied to understand the relative roles of dynamic (circulation) and thermodynamic (moisture) processes in causing the difference of the precipitation DC between boreal winter and summer. The column-integrated moisture budget equation may be written as (Banacos and Schultz 2005)

$$\Delta(P^*) = \Delta(E^*) - \Delta\left(\left\langle\frac{\partial q}{\partial t}\right\rangle^*\right) - \Delta(\langle q\nabla\cdot\mathbf{V}_h\rangle^*) - \Delta(\langle\mathbf{V}_h\cdot\nabla q\rangle^*), \quad (1)$$

where $\mathbf{V}_h$ denotes the horizontal wind vector, $E$ denotes the surface evaporation, $q$ denotes the specific humidity, $\nabla$ represents the horizontal gradient operator, an asterisk denotes the diurnal range defined as the rainfall difference between 1500–1800 LST (0600–0900 LST) and 0600–0900 LST (1500–1800 LST) over land (ocean), $\Delta$ denotes the seasonal difference between boreal winter and summer (i.e., DJF minus JJA), and angle brackets represent the vertical integration from 1000 hPa to 100 hPa. The second term on the right-hand side of Eq. (1) may be omitted because its magnitude is much smaller than the rainfall rate. Thus we have

$$\Delta(P^*) = \Delta(E^*) - \Delta(\langle q\nabla\cdot\mathbf{V}_h\rangle^*) - \Delta(\langle\mathbf{V}_h\cdot\nabla q\rangle^*), \quad (2)$$

By decomposing each variable into a seasonal mean, a diurnal and a residual component (i.e., $= \overline{A} + A' + A''$) (Hsu et al.

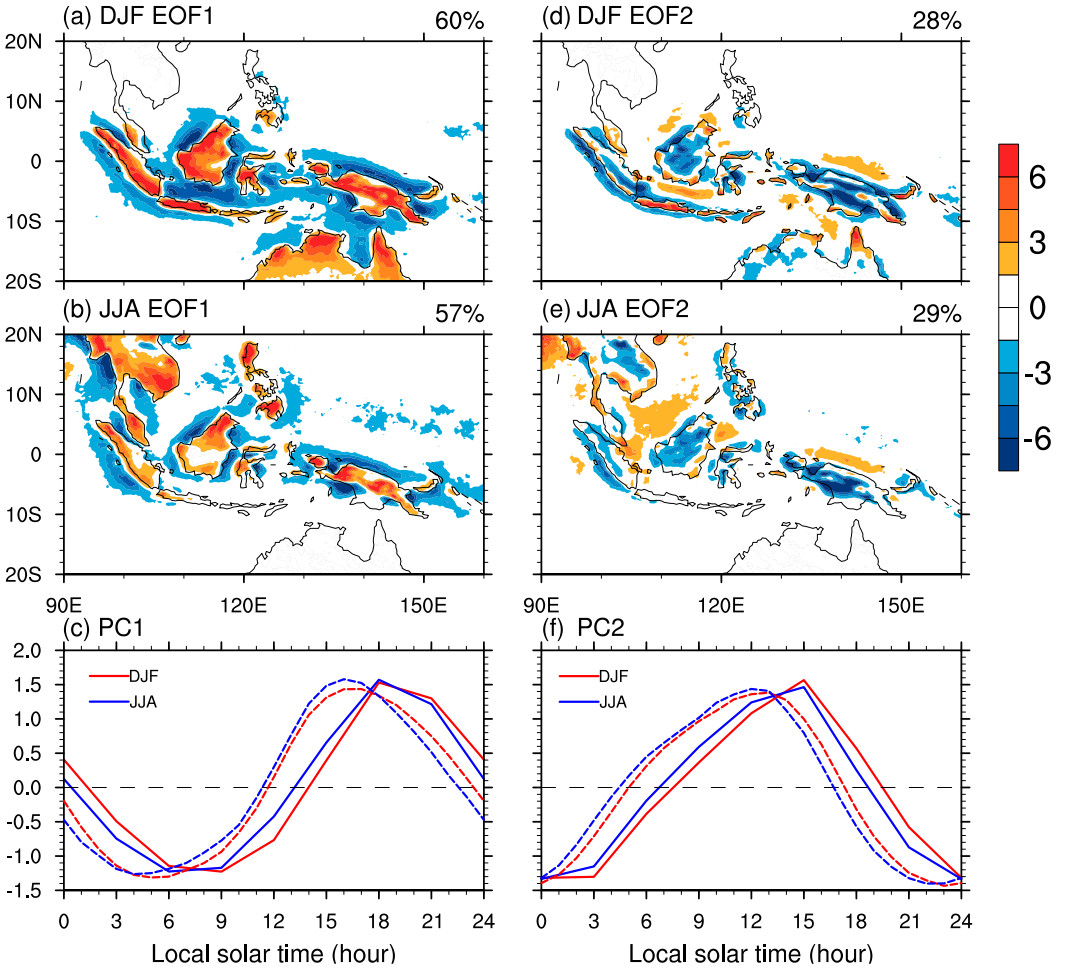


FIG. 3. The leading two EOF modes of precipitation DC averaged over different seasons: (a) EOF1 for DJF, (b) EOF1 for JJA, and (c) PC1 for DJF (red line) and JJA (blue line). (d)–(f) As in (a)–(c), but for EOF2 and PC2. The spatial patterns and the solid lines are derived from 3B42, whereas the dashed lines are derived from 3G68 (mm day$^{-1}$).

2011; Wang et al. 2017, 2019), one may derive the moisture convergence and advection terms in Eq. (2) as the following:

$$-\Delta(\langle q\nabla\cdot\mathbf{V}_h\rangle^*) = -\Delta(\langle \overline{q}\nabla\cdot\overline{\mathbf{V}}_h + \overline{q}\nabla\cdot\mathbf{V}'_h + \overline{q}\nabla\cdot\mathbf{V}''_h + q'\nabla\cdot\overline{\mathbf{V}}_h + q'\nabla\cdot\mathbf{V}'_h + q'\nabla\cdot\mathbf{V}''_h + q''\nabla\cdot\overline{\mathbf{V}}_h + q''\nabla\cdot\mathbf{V}'_h + q''\nabla\cdot\mathbf{V}''_h\rangle^*), \quad (3)$$

$$-\Delta(\langle \overline{V}_h\cdot\nabla q\rangle^*) = -\Delta(\langle \overline{V}_h\cdot\nabla\overline{q} + \overline{V}_h\cdot\nabla q' + \overline{V}_h\cdot\nabla q'' + \mathbf{V}'_h\cdot\nabla\overline{q} + \mathbf{V}'_h\cdot\nabla q' + \mathbf{V}'_h\cdot\nabla q'' + \mathbf{V}''_h\cdot\nabla\overline{q} + \mathbf{V}''_h\cdot\nabla q' + \mathbf{V}''_h\cdot\nabla q''\rangle^*). \quad (4)$$

In the equations above, the overbar variable uses either the boreal winter or summer mean state, the primed variable is obtained from a 1.5-day high-pass filtering, and the double-primed variable is obtained by subtracting the season mean and the diurnal components from the total field. The terms in Eqs. (3) and (4) were calculated based on the MERRA inst3_3d_asm_Cp dataset.

### c. Model configuration

The Advanced Research Weather Research and Forecasting Model (WRF-ARW, version 4.0) with a 25-km horizontal resolution is used to simulate the precipitation DC in this study. The model top was set at 50 hPa with 40 layers in the vertical. The simulation covers most of the MC and the domain consists of 394 × 177 grid points (short-dashed box in Fig. 1). The climatological states of boreal winter and summer are constructed using the European Centre for Medium-Range Weather Forecasts interim reanalysis (ERA-Interim) data with a resolution of 0.5° × 0.5° at 6-h intervals (Uppala et al. 2008), and used as initial and lateral boundary conditions.

The simulations utilize various physical parameterizations. These include the Kain–Fritsch convective parameterization scheme, the Yonsei University (YSU) boundary layer scheme, WRF single-moment 6-class graupel, the RRTM longwave radiation and the Dudhia shortwave radiation schemes, the Monin–Obukhov

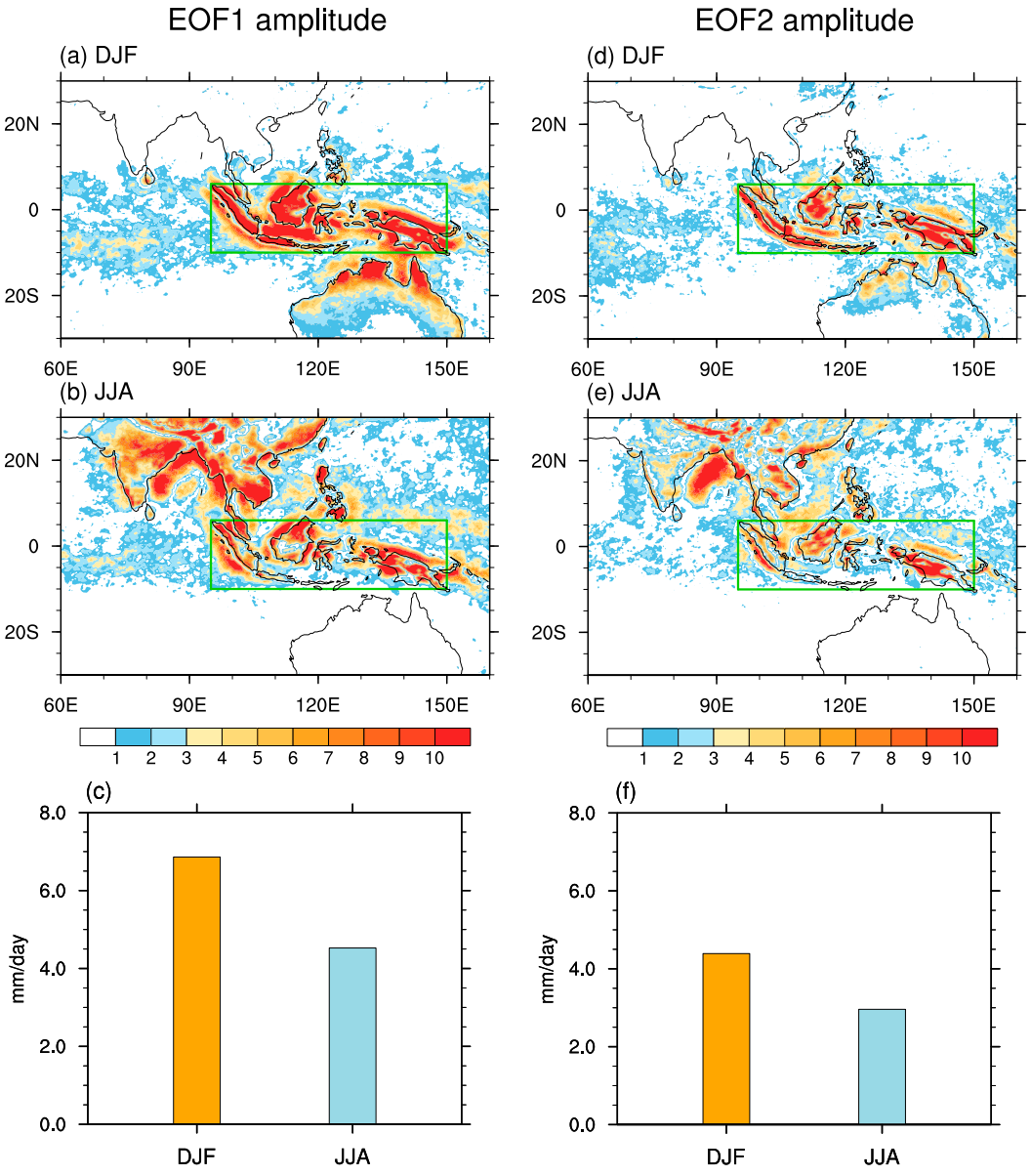


FIG. 4. EOF1 amplitude (mm day$^{-1}$) composite for (a) DJF and (b) JJA. The green box denotes the MMC area (10°S–6°N, 95°–150°E). (c) The MMC-averaged EOF1 amplitude (mm day$^{-1}$) composite for DJF (orange bar) and JJA (light blue bar). (d)–(f) As in (a)–(c), respectively, but for EOF2 amplitude.

surface-layer scheme, and the unified Noah land surface model scheme. Such parameterizations were used by Du and Rotunno (2018) to investigate the characteristics and mechanisms of diurnal rainfall and winds near the south coast of China and could be used to capture the diurnal propagation signals off the east coast of China (Du and Rotunno 2015).

We performed a control experiment and four sensitivity experiments. The control experiment (CTL) was designed for the wet season in the MC (i.e., DJF). The 17-yr-averaged DJF mean state including surface pressure, wind fields, geopotential height, temperature, SST, and specific humidity was used as the initial and lateral boundary conditions (Cao et al. 2014). Sensitivity experiments were conducted and results were compared with the control experiment to identify impacts of moisture, temperature, and circulation on the amplitude of precipitation DC. In EXP1, the area-averaged vertical profile of specific humidity in JJA was specified while other variables remain the same as in the control experiment. This experiment was specially designed to reveal the moisture effect. In EXP2, the area-averaged temperature vertical profile in JJA was specified while the specific humidity and other circulation variables remain the same as in the control experiment. This experiment is to examine the pure effect of atmospheric static stability. In EXP3, the circulation field in JJA was specified while the area-averaged vertical

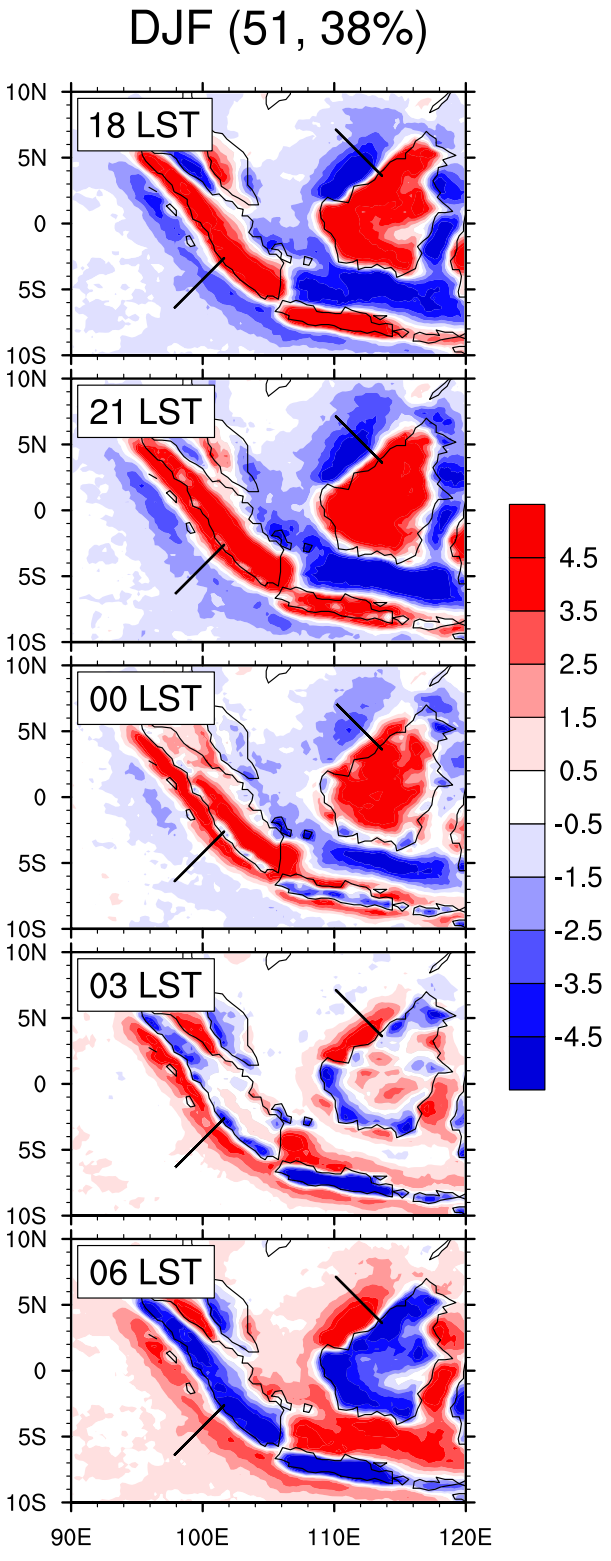


FIG. 5. Evolution of precipitation represented by the combination of EEOF1 and EEOF2 for DJF over the western MC. See the text for the complete description of the procedure. The corresponding LSTs are shown at the top-left corner of panels. Diagonal black lines indicate offshore propagation.

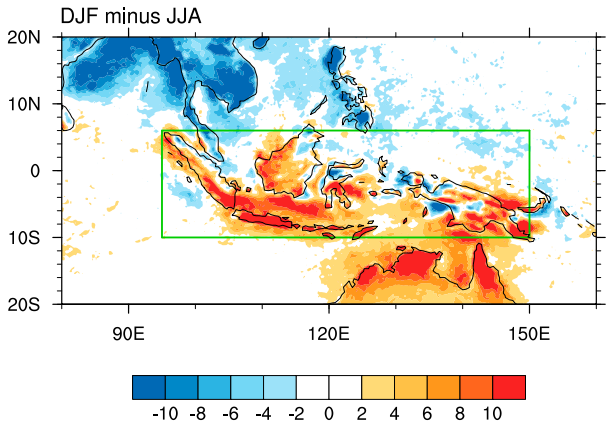


FIG. 6. Difference in diurnal range of precipitation (mm day$^{-1}$) between DJF and JJA (DJF minus JJA). Results passing the significant test at 95% confidence level are presented. The green box denotes the MMC area (10°S–6°N, 95°–150°E).

profiles of specific humidity and temperature are the same as those in the control experiment. By comparing the simulations between this experiment with the CTL, one may reveal the circulation effect. In EXP4, all dynamic and thermodynamic fields were replaced by the JJA mean state. The model was run for 90 days for all the experiments above.

## 3. Observed features of precipitation DC in boreal winter and summer

Figure 2 shows the horizontal patterns and principal components of the leading two EOF modes of the annual mean precipitation DC for the period of 1998–2014. Both the TRMM 3B42 and 3G68 datasets were used. The first EOF mode explains 53%–58% of the total variance, with a clear land–sea contrast with positive (negative) values over land (ocean) (Figs. 2a,d). The corresponding principal component (PC1; Fig. 2c) derived from 3B42 shows a clear diurnal cycle with a peak in the early evening (1800 LST) over land and in the morning (0900 LST) over ocean. The leading EOF mode reflects a typical DC over the MC in association with the DC of land surface heat flux due to solar heating and longwave radiative cooling. The second EOF mode (Figs. 2b,e) explains 27%–30% of the total variance, and reflects a complementary geographical variation, which represents a component deviating from the typical DC. This diurnal mode is possibly attributed to the modulation of island shape and terrain height and orientation. It may somehow relate to the interaction of the DC with gravity waves, density currents, and local circulations around coasts and mountains (Kikuchi and Wang 2008; Qian 2008; Rauniyar and Walsh 2011; Teo et al. 2011). Comparing to the diurnal signal over open oceans, the signal over land and coastal region is stronger because it has a larger magnitude of the eigenvectors in both EOFs.

The horizontal patterns of the leading EOF modes from the 3G68 contain similar characteristics. However, the principal components derived from 3G68 lead those from 3B42 by 2–3 h (Figs. 2c,f), due to the fact that the former was a direct

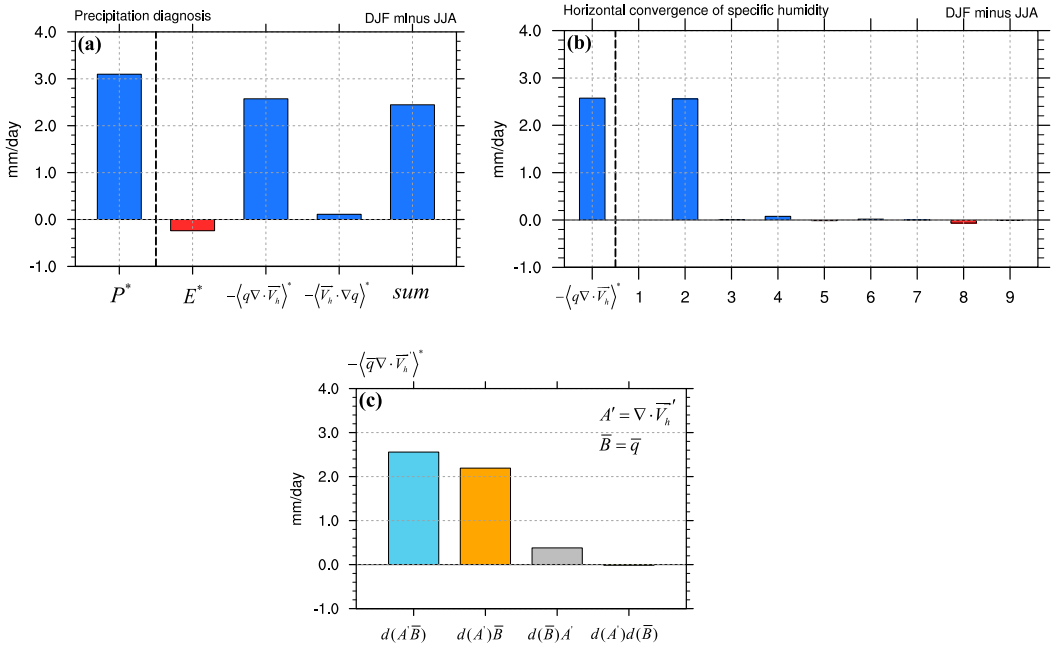


FIG. 7. (a) Vertically integrated (1000–100 hPa) precipitation budget terms (mm day$^{-1}$) of difference in diurnal range between DJF and JJA averaged over the MMC (10°S–6°N, 95°–150°E). (b) Decomposition of various horizontal moisture convergence components in the precipitation budget. Right of the dashed line are as follows: $-\Delta(\langle\overline{q}\nabla\cdot\overline{\mathbf{V}_h}\rangle^*)$ (bar 1), $-\Delta(\langle\overline{q}\nabla\cdot\mathbf{V}_h'\rangle^*)$ (bar 2), $-\Delta(\langle\overline{q}\nabla\cdot\mathbf{V}_h''\rangle^*)$ (bar 3), $-\Delta(\langle q'\nabla\cdot\overline{\mathbf{V}_h}\rangle^*)$ (bar 4), $-\Delta(\langle q'\nabla\cdot\mathbf{V}_h'\rangle^*)$ (bar 5), $-\Delta(\langle q'\nabla\cdot\mathbf{V}_h''\rangle^*)$ (bar 6), $-\Delta(\langle q''\nabla\cdot\overline{\mathbf{V}_h}\rangle^*)$ (bar 7), $-\Delta(\langle q''\nabla\cdot\mathbf{V}_h'\rangle^*)$ (bar 8), and $-\Delta(\langle q''\nabla\cdot\mathbf{V}_h''\rangle^*)$ (bar 9). (c) Relative contributions of the diurnal wind change and the seasonal mean moisture change to term 2 in (b). For this term, four columns represent $d(A'\overline{B})$, $d(A')\overline{B}$, $d(\overline{B})A'$, and $d(A')d(\overline{B})$, respectively. Here $d(\ )$ indicates the change from DJF to JJA, $A'$ denotes the diurnal wind divergence, and $\overline{B}$ denotes the seasonal mean moisture.

observation of precipitation, whereas the latter was estimated from TRMM Microwave Imager (TMI) and infrared (IR), and the time of occurrence of maximum rainfall in IR-estimated rainfall is strongly affected by cloud cover and tends to lag behind in situ observations by approximately 3 h (Kubota and Nitta 2001). Previous studies suggested to use the temporal phase from 3G68 because of its higher temporal sampling but to use the spatial pattern from 3B42 because of its larger spatial sampling (e.g., Kikuchi and Wang 2008; Wang et al. 2011). Rauniyar and Walsh (2011) also discussed the time evolution difference from both the datasets. Since the precipitation peaks occur in a time range based on the two datasets, hereafter we simply use the ensemble mean of the two datasets to describe the observed DC phase with a peak phase at 1500–1800 LST (0600–0900 LST) over land (ocean).

By applying the same analysis method to the precipitation DC in different seasons, we find that the largest difference appears between DJF and JJA (figure not shown). Therefore, boreal winter and summer seasons are selected to investigate the seasonal contrast of precipitation DC. Figure 3 shows the patterns and principal components of the two leading EOFs in DJF and JJA, respectively. EOF1 (EOF2) explains about 60% (30%) of the total variance in both the seasons. It is clearly seen that both the geographical distribution and time series of the leading two EOF modes in DJF and JJA are quite similar. The major difference lies in the amplitude, with significantly larger amplitudes during DJF over the MC major islands and adjacent oceans.

To clearly illustrate the amplitude difference between boreal winter and summer, we plotted the horizontal distributions of EOF1 and EOF2 amplitude (Fig. 4). Note that both the EOF1 and EOF2 amplitudes are greater in boreal winter than in boreal summer, especially over the major islands and adjacent oceans. Figures 4c and 4f display the EOF1 and EOF2 amplitudes averaged over the MC major islands and adjacent oceans (MMC; 10°S–6°N, 95°–150°E) in DJF and JJA. The average EOF1 amplitude in DJF is 6.9 mm day$^{-1}$, whereas it becomes 4.5 mm day$^{-1}$ in JJA, reducing by 35% from its DJF counterpart. The EOF2 amplitude shows a similar reduction rate, with an averaged value of 4.4 mm day$^{-1}$ in DJF and 2.9 mm day$^{-1}$ in JJA.

To better capture the diurnal rainfall propagation feature, an extended EOF (EEOF) analysis similar to that of Kikuchi and Wang (2008) was conducted. The EEOF was performed on the 3B42 with two lags of ±3 h. The constructed figure (Fig. 5) shows a half of the diurnal precipitation cycle from 1800 to 0600 LST. The counterpart half cycle can be expressed by patterns with the signs opposite to Fig. 5. Because similar propagation features appear in JJA, here we only show the DJF result. As shown in Fig. 5, the maximum diurnal precipitation occurs over the Sumatra land at 1800 LST, and then it propagates offshore with time over the west coast of Sumatra Island. At 0600 LST, the precipitation center appears about 200 km away from the coast. Over the northwest coast of

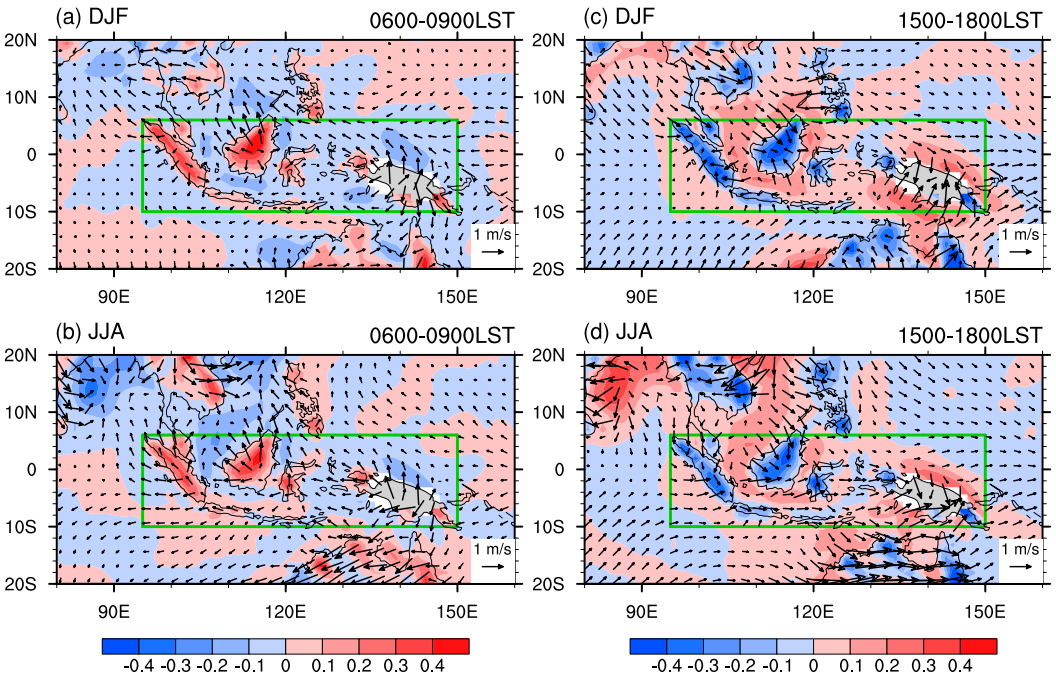


FIG. 8. Horizontal distributions of 950–850-hPa-averaged diurnal wind (vectors; $\mathrm{m\,s^{-1}}$) and the associated divergence (shading; $10^{-5}\,\mathrm{s^{-1}}$) composite for (a),(c) DJF and (b),(d) JJA during (left) 0600–0900 and (right) 1500–1800 LST. The green boxes mark the MMC area (10°S–6°N, 95°–150°E).

Borneo, the offshore propagation is also clearly seen. These propagation features are consistent with previous studies (e.g., Mori et al. 2004; Ichikawa and Yasunari 2006, 2008; Kikuchi and Wang 2008). While the propagation feature is similar between DJF and JJA, the main difference lies in the magnitude, which is closely associated with the DC amplitude. Therefore, we will focus on examining the seasonal difference of DC amplitude in the following.

The amplitude difference may be measured by the diurnal range of precipitation, which is defined as the difference of rainfall rate between 1500–1800 LST (0600–0900 LST) and 0600–0900 LST (1500–1800 LST) over land (ocean). The horizontal pattern of the diurnal range difference between DJF and JJA, i.e., DJF minus JJA, is shown in Fig. 6. It is clearly seen that the diurnal range is greater in boreal winter than in boreal summer in the MMC. The regions with large diurnal range differences appear in the MMC where the diurnal range of precipitation is large. The difference over land and coastal oceans is larger than that over open oceans. The same result was obtained when a different definition of the diurnal range (based on daily maximum and minimum precipitation; Kikuchi and Wang 2008) was used. The pattern correlation coefficients between results from the two different diurnal range definitions are about 0.9, and are statistically significant above a 95% confidence level.

## 4. Mechanisms for annual cycle modulation on DC

An interesting question is what causes the DC amplitude difference between boreal summer and winter? To address this question, we first perform a vertically integrated (1000–100 hPa) moisture budget analysis over the MMC.

Figure 7a shows the contribution from each of the vertically integrated moisture budget terms. The cause of a positive anomaly in $\Delta(P^*)$, which represents a larger diurnal range of precipitation during DJF compared to JJA, is primarily attributed to the vertically integrated horizontal moisture convergence term [i.e., $-\Delta(\langle q\nabla\cdot\mathbf{V}_h\rangle^*)$]. In addition to the convergence effect, the evaporation and horizontal moisture advection both contribute quite little and the contribution from evaporation is negative. If one separates the vertically integrated horizontal moisture convergence term according to Eq. (3), one may find that the leading term comes from the horizontal convergence of the seasonal mean moisture by diurnal wind [i.e., term2: $-\Delta(\langle\overline{q}\nabla\cdot\mathbf{V}_h'\rangle^*)$], while the other terms all contribute quite limited (Fig. 7b).

Given that both the seasonal mean moisture change and the diurnal wind change from DJF to JJA contribute to the change of horizontal moisture convergence term, we next examine specific processes that give rise to the positive difference in the horizontal moisture convergence. Figure 7c displays their relative contributions based on the total differential relationship (Chen et al. 2015):

$$d(A'\overline{B}) = d(A')\overline{B} + A'd(\overline{B}) + d(A')d(\overline{B}), \tag{5}$$

where $d(\ )$ indicates the change from DJF to JJA (i.e., DJF minus JJA), $A'$ denotes the diurnal part, and $\overline{B}$ denotes the seasonal mean part. Equation (5) states that the change of the product of $A'$ and $\overline{B}$ can be decomposed into three parts. The

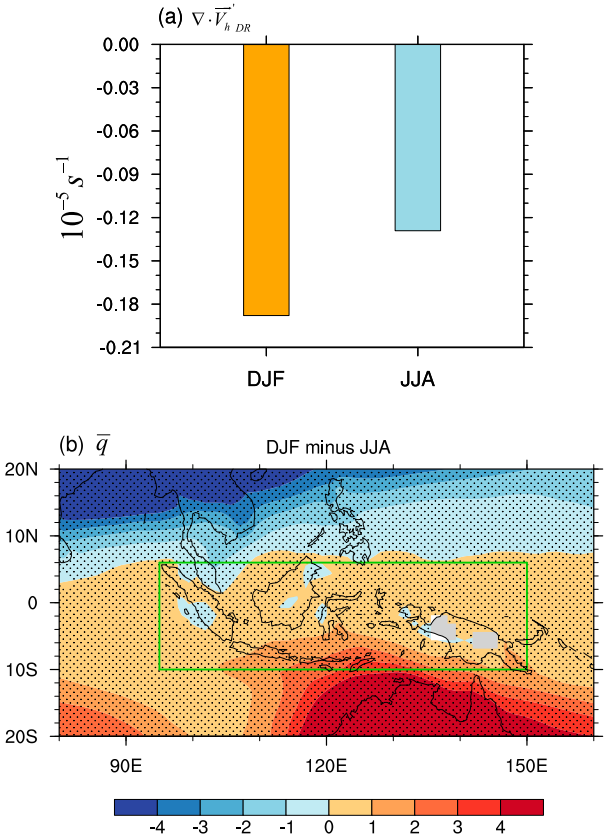


FIG. 9. (a) The MMC-averaged diurnal range of wind divergence ($10^{-5}\,s^{-1}$) over 950–850-hPa composite for DJF (orange bar) and JJA (light blue bar). (b) Difference in composite 950–850-hPa-averaged seasonal mean specific humidity ($g\,kg^{-1}$) between DJF and JJA (DJF minus JJA). Dots denote regions above the 95% confidence level. The green box denotes the MMC area (10°S–6°N, 95°–150°E).

first part is attributed to the change in diurnal wind, the second part is attributed to the change in seasonal mean moisture, and the third part is the residual part related to covariance between the seasonal mean moisture and diurnal wind changes. Note that the major contributor to the change in the convergence of seasonal mean moisture by diurnal wind $[-\Delta(\langle\overline{q}\nabla\cdot\mathbf{V}_h'\rangle^*)]$ lies in the change in diurnal wind (i.e., $\mathbf{V}_h'$), which accounts for about 85%, while the change in seasonal mean moisture has a much smaller contribution.

The horizontal patterns of 950–850-hPa-averaged diurnal wind and divergence fields at 0600–0900 and 1500–1800 LST are shown in Fig. 8. In both the seasons, the diurnal wind tends to converge over ocean and diverge over land in the morning, and acts oppositely in the afternoon. It corresponds well to the diurnal change of precipitation shown in Fig. 3. While their horizontal patterns are quite similar, their amplitudes differ between the winter and summer.

Figure 9a compares the diurnal range of the wind divergence averaged over the MMC during DJF and JJA. The diurnal range of the divergence is calculated by the 950–850-hPa-averaged diurnal wind divergence during 1500–1800 LST (0600–0900 LST) minus that during 0600–0900 LST (1500–1800 LST) over land (ocean), in a way similar to the calculation of diurnal range of precipitation. It is found that the diurnal range of the low-level wind convergence decreases by about 35% in JJA compared to DJF.

What causes the stronger diurnal wind variability over the MC in DJF that helps strengthen precipitation DC? Figure 9b presents the difference in 950–850-hPa-averaged seasonal mean moisture between DJF and JJA. One can see clearly that a greater background moisture condition appears in the MMC during DJF. The vertical profiles of vertical velocity, divergence, zonal wind, relative humidity, and temperature anomaly averaged over the MMC during DJF and JJA are displayed in Fig. 10. A stronger ascending motion, low-level convergence, and upper-level divergence appear during DJF compared to JJA. As stronger easterly shear (Wang and Xie 1996), larger relative humidity, and stronger static instability are all favorable environmental conditions for the perturbation growth (solid lines in Figs. 10a–d), it is desirable to investigate the relative roles of the background dynamic and thermodynamic fields in generating the stronger diurnal variability over the MC.

To address the issue above, we design a set of idealized numerical experiments using the WRF Model, with a focus on evaluating the simulated rainfall DC. Comparisons are made between diurnal composites derived from the WRF simulations for DJF and JJA. Figure 11 shows the results of the EOF analysis from the WRF simulation and the corresponding EOF1 and EOF2 amplitude averaged over the MMC. Note that there is general similarity in EOF1 spatial patterns in DJF and JJA. The contrast of precipitation DC represented by EOF1 over the land and sea is clearly seen. The WRF simulation also shows good agreement in the temporal phase with the TRMM observation. The simulated precipitation DC peaks at 1600 LST over land and around 0600 LST over ocean. The EOF2 spatial patterns and temporal phase in DJF and JJA are also well simulated, especially for the rainfall signal off the west coast of Sumatra and the northwest coast of Borneo. In addition, the amplitude difference ratios between boreal winter and summer for both the EOF modes are well captured (Figs. 11d,h), compared to the observed.

To compare the simulated offshore propagating feature with the observed, we conducted the same EEOF analysis for the WRF simulation. As shown in Fig. 12, the offshore rainfall propagation in DJF over the coasts of Sumatra and Borneo is to a large extent captured by the model, even though there is a bias in the timing of the diurnal precipitation near the coast. A similar propagation appears in JJA with a weaker amplitude (figure not shown).

Given that the model is capable of simulating the distinctive contrast between boreal winter and summer, different combinations of seasonal mean moisture, temperature, and circulation fields are then prescribed in order to examine their relative roles. Detailed experiment setup is depicted in section 2c. Here we also use the diurnal range to identify the amplitude of precipitation DC. Averaging over the MC

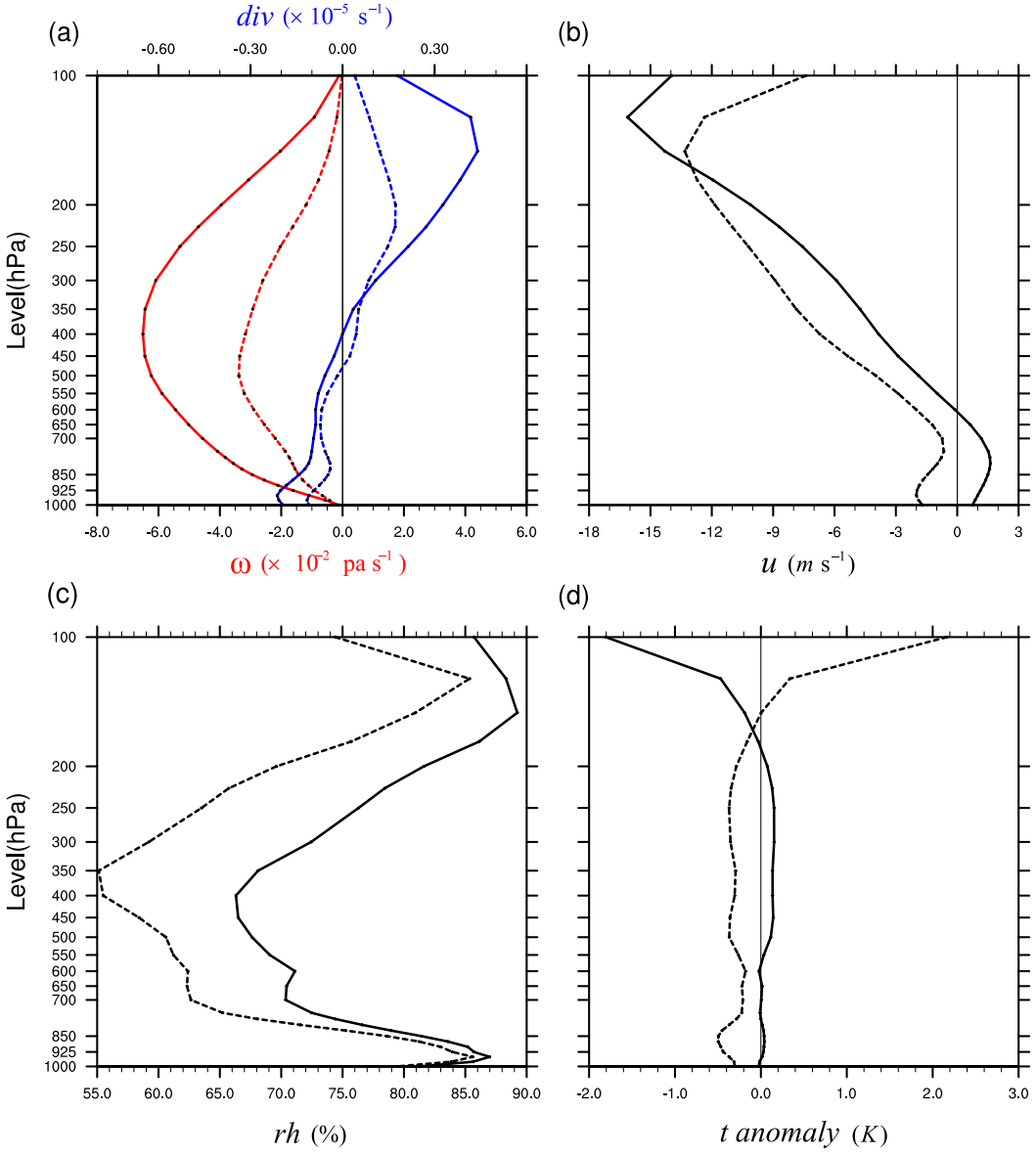


FIG. 10. Vertical profiles of (a) vertical velocity (red) and divergence (blue), (b) zonal wind, and (c) relative humidity averaged over the MMC (10°S–6°N, 95°–150°E) during DJF (solid) and JJA (dashed). (d) As in (a)–(c), but for temperature anomaly. The solid lines represent difference between DJF and the annual mean and the dashed lines denote difference between JJA and the annual mean.

region, one may calculate the relative contribution of moisture, atmospheric static stability, and circulation to the rainfall DC amplitude change (Fig. 13). It is clearly seen that the amplitude difference with the CTL is largest in EXP4, followed by EXP1, EXP2, and EXP3. This indicates that the main factor that affects the distinctive seasonal contrast of precipitation DC between boreal winter and summer is the vertical profile of specific humidity. The second important factor is atmospheric stability or area-mean vertical temperature profile, whereas the third factor is the circulation. The ratios of the moisture, temperature, and circulation contributions are 59%, 26%, and 15%.

In the previous experiments, a time-dependent lateral boundary condition was specified. To examine the sensitivity of the model result to the choice of lateral boundary condition, experiments with a fixed seasonal mean lateral boundary condition were carried out, and a similar result was obtained, with the ratios of the moisture, temperature and circulation contributions being 61%, 25%, and 14%, respectively (figure not shown). Thus one may conclude that the seasonal mean background moisture condition is most critical in modulating the annual cycle of precipitation DC over the MC, followed by the seasonal mean atmospheric static stability and circulation fields.

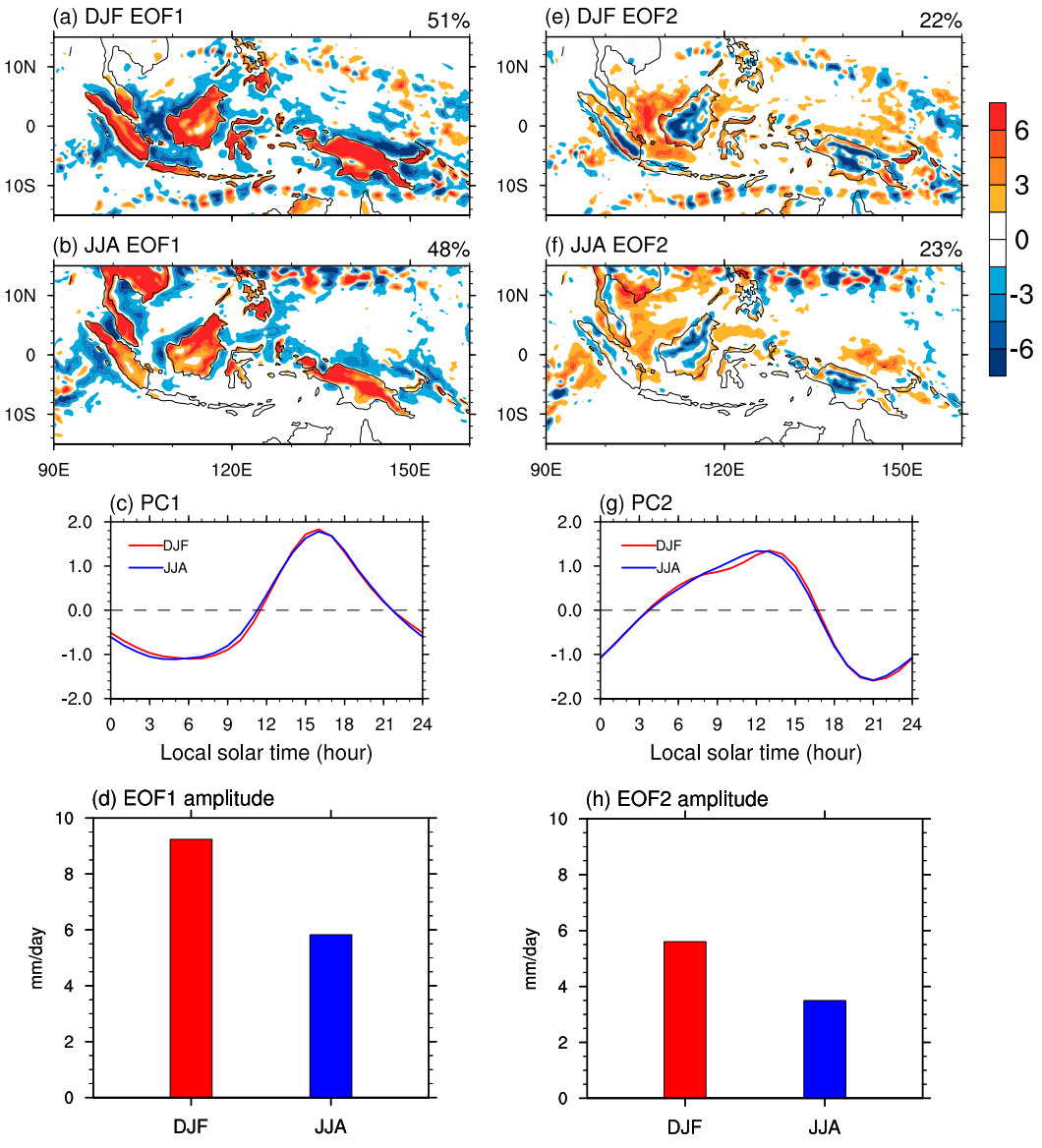


FIG. 11. The leading two EOF modes of precipitation DC averaged over different seasons derived from WRF simulations: (a) EOF1 for DJF, (b) EOF1 for JJA, (c) PC1 for DJF (red line), and JJA (blue line). (d) The MMC (10°S–6°N, 95°–150°E)-averaged EOF1 amplitude (mm day$^{-1}$) composite for DJF and JJA derived from WRF simulations. (e)–(h) As in (a)–(d), respectively, but for EOF2.

To connect to the moisture budget analysis, we also examine the diurnal wind and the associated divergence. Figure 14 displays the area-averaged diurnal range of the diurnal wind divergence at low levels (averaged at 950–850 hPa) for the controlled and sensitivity experiments. The diurnal range of the low-level wind divergence matches the diurnal range of precipitation, which is largest in CTL, followed by EXP3, EXP2, EXP1, and smallest in EXP4.

Based on the precipitation budget diagnosis and the numerical experiments above, a mechanism for the modulation of precipitation DC by climatological annual cycle is proposed. This mechanism can be summarized as follows. Assume that the diurnal wind perturbation has the same amplitude initially. A greater background mean moisture during DJF results in a stronger condensational heating on the diurnal scale, which further enhances the diurnal wind activity and strengthens the precipitation DC amplitude. Meanwhile, the background mean static stability and circulation are also favorable for the growth of the perturbation wind activity in DJF. Therefore, the favorable seasonal-mean atmospheric thermodynamic and dynamic conditions in DJF promote a positive circulation–convection feedback on the diurnal time scale to enhance the precipitation DC activity (Lu et al. 2019). Opposite processes operate during JJA.

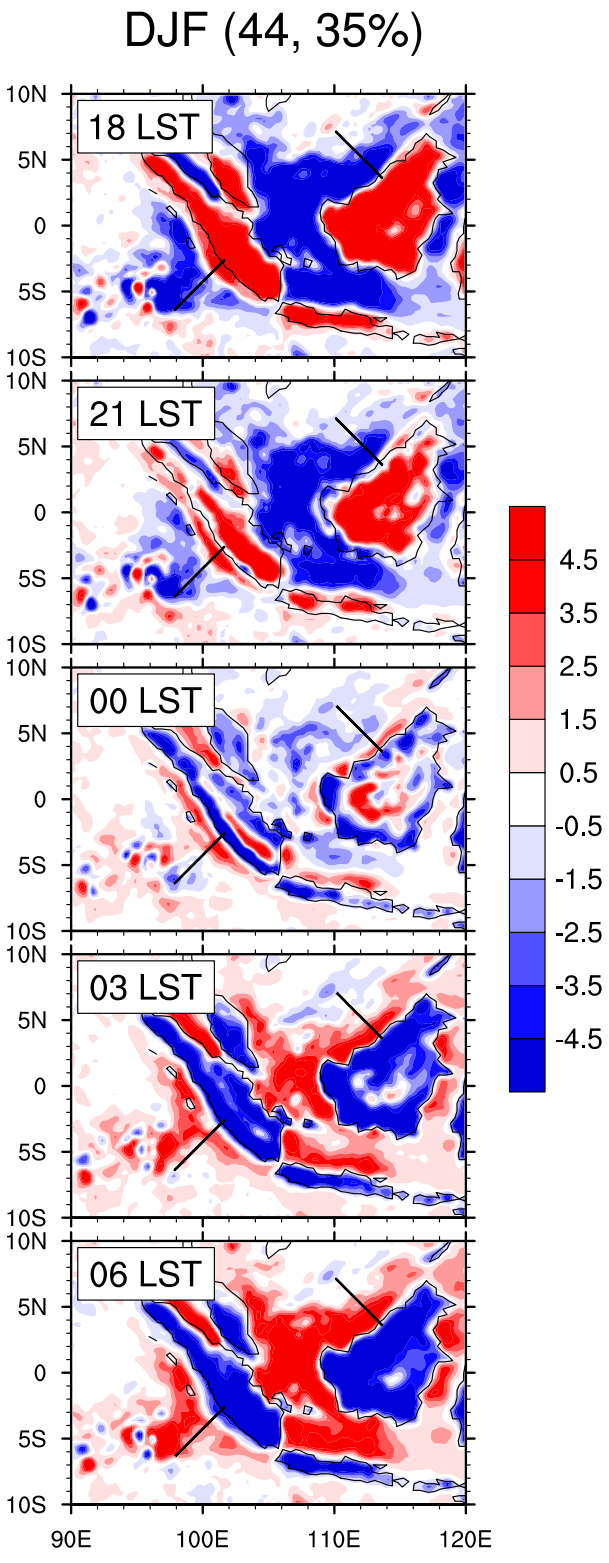


FIG. 12. Evolution of WRF-simulated precipitation represented by the combination of EEOF1 and EEOF2 for DJF over the western MC. The corresponding LSTs are shown at the top-left corner of panels. Diagonal black lines indicate offshore propagation.

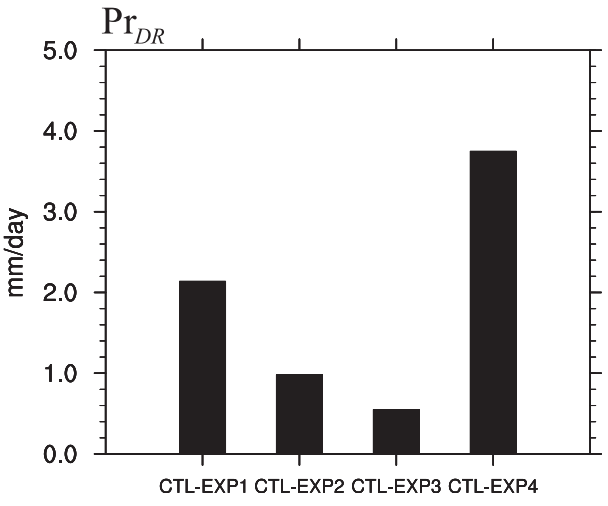


FIG. 13. Difference of MMC-averaged (10°S–6°N, 95°–150°E) diurnal range of precipitation (mm day$^{-1}$) between the control experiment and various sensitivity experiments. From left to right, the bars represent CTL minus EXP1, CTL minus EXP2, CTL minus EXP3, and CTL minus EXP4, respectively.

## 5. Conclusions and discussion

In this study, we examined the influences of the background mean annual cycle on the precipitation DC over the MC. The precipitation DC for the period of 1998–2004 is examined in boreal winter and summer seasons.

The EOF analysis during boreal winter and summer seasons shows that the difference in precipitation DC between the two seasons is statistically significant. There is no recognizable distinction in the pattern and time evolution of precipitation DC between DJF and JJA. The precipitation DC tends to peak in the afternoon (1500–1800 LST) over land and in the morning

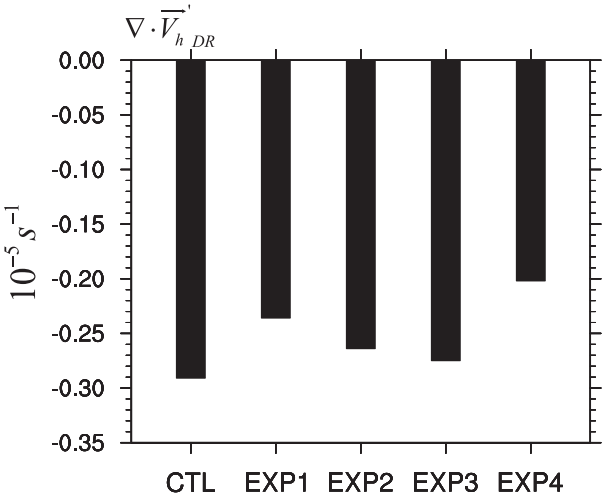


FIG. 14. The MMC-averaged (10°S–6°N, 95°–150°E) diurnal range of wind divergence ($10^{-5}$ s$^{-1}$) over the 950–850-hPa composite for the control experiment and various sensitivity experiments.

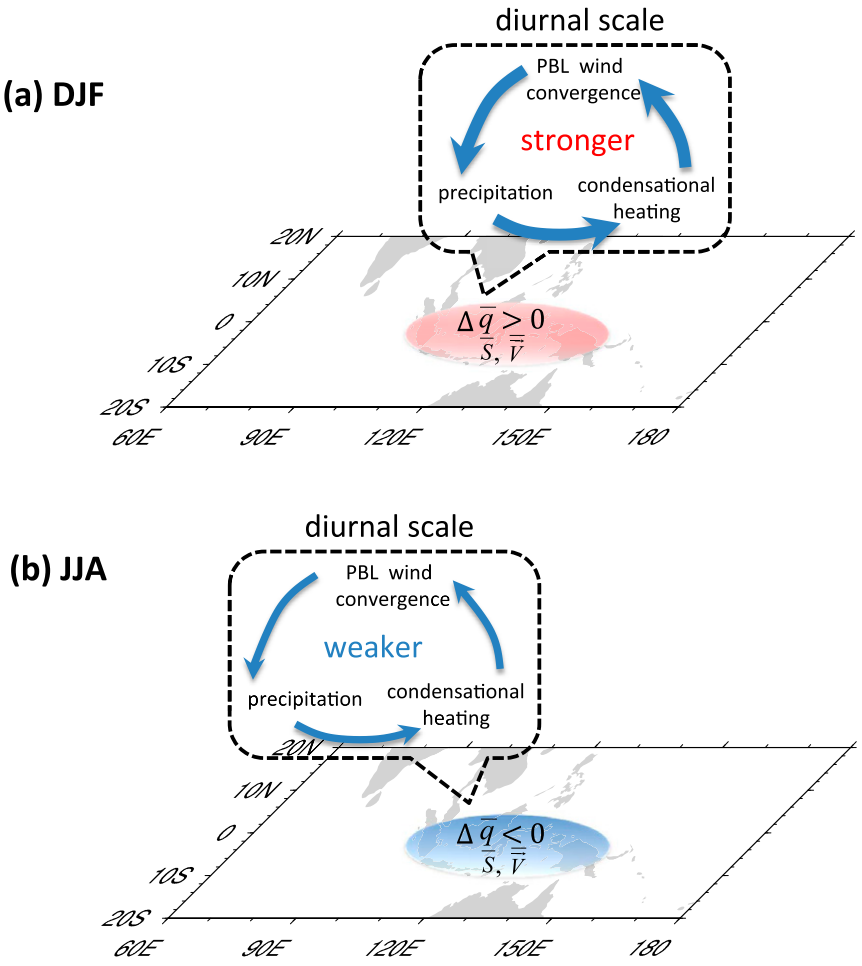


FIG. 15. Schematic diagram illustrating the mechanism of precipitation DC over the MC modulated by the climatological annual cycle during (a) DJF and (b) JJA. $\Delta\overline{q}$, $\overline{S}$, and $\overline{\mathbf{V}}$ represent seasonal mean moisture, instability, and circulation, respectively. The dotted boxes in (a) and (b) represent stronger and weaker positive circulation–convection feedback processes on the diurnal scale, respectively.

(0600–0900 LST) over coastal ocean during both the seasons. The difference mainly arises from the amplitude of precipitation DC, which reduces by about 35% in JJA compared to DJF. The propagation feature is similar between DJF and JJA, the main difference lies in the magnitude.

An analysis of the vertically integrated precipitation budget over the MC indicates that the horizontal moisture convergence term [i.e., $-\Delta(\langle q\nabla\cdot\mathbf{V}_h\rangle^*)$] dominates and is the major term affecting the winter–summer difference. A further decomposition shows that the leading term is the convergence of the seasonal mean moisture by diurnal wind [i.e., $-\Delta(\langle\overline{q}\nabla\cdot\mathbf{V}_h'\rangle^*)$]. The relative role of the seasonal mean moisture and the diurnal wind was further examined. It is found that the major contributor lies in the diurnal wind (i.e., $\mathbf{V}_h'$). The difference in the diurnal wind field between DJF and JJA lies in their intensity, not their pattern. The diurnal range of low-level wind convergence decreases by about 35% in JJA compared to DJF. The cause of the diurnal wind intensity difference, however, is ultimately attributed to the difference of the seasonal mean state between boreal winter and summer.

Sensitivity numerical experiments with the WRF Model were conducted to investigate the relative roles of the background dynamic and thermodynamic fields in generating the distinctive seasonal contrast of the precipitation DC over the MC. The results indicate that the background moisture field is most important (~60%), followed by the atmospheric static stability contribution (~25%) and the circulation contribution (~15%).

The schematic diagram in Fig. 15 summarizes the mechanism through which the seasonal cycle mean state modulates the DC amplitude. In boreal winter, the seasonal mean moisture anomaly (relative to the annual mean state) is positive over the MC major islands and adjacent oceans, which provides more energy for the diurnal cycle perturbation to grow. In boreal summer, the seasonal mean moisture anomaly is negative over the MC major islands and adjacent oceans, which provides less energy for the diurnal cycle perturbation. The

increase of the background moisture, along with the favorable static stability and circulation conditions in boreal winter, strengthens a positive circulation–convection–moisture feedback on the diurnal time scale, increasing the amplitude of the diurnal wind and precipitation.

This study discusses the relative roles of the background dynamic and thermodynamic states in causing the seasonal difference in precipitation DC by the WRF Model, while it is worth mentioning that the seasonal mean moisture difference is caused by the difference of the seasonal mean monsoon circulation, and that even though the circulation difference shows less sensitivity in the WRF modeling results, it does not mean that it is not important in regulating the seasonal difference of the diurnal precipitation. While this study provides insights into the physical processes controlling the interactions between diurnal precipitation and the climatological annual cycle over the MC, further analyses are required to reveal the similarities and differences between the physical mechanisms behind the modulation of the DC by different large-scale climate variabilities. Some mechanisms of how large-scale climate variabilities could impact the DC over the MC have been proposed (Rauniyar and Walsh 2011, 2013; Peatman et al. 2014, 2015; Baranowski et al. 2016; Birch et al. 2016; Sakaeda et al. 2017, 2018; Hung and Sui 2018); however, no consensus has been reached. Therefore, the roles of moisture, radiation, static stability, large-scale circulation, and cloud life cycles, etc., along with their interactions, need to be examined under different large-scale background states in greater detail in the future to understand the physical mechanisms that modulate the DC over the MC.

*Acknowledgments.* This work was supported by China National Key S&T project 2018YFC1505801, NSFC Grants 41875069, 41575043, 41705059, and 41975108; NOAA Grant NA18OAR4310298; and NSF Grant AGS-16-43297. The numerical calculations in this paper have been done on the supercomputing system in the Supercomputing Center of Nanjing University of Information Science & Technology. This is SOEST contribution number 11193, IPRC contribution number 1488, and ESMC contribution number 336.

## REFERENCES

As-syakur, A. R., and Coauthors, 2019: Analysis of spatial and seasonal differences in the diurnal rainfall cycle over Sumatera revealed by 17-year TRMM 3B42 dataset. *SOLA*, **15**, 216–221, https://doi.org/10.2151/sola.2019-039.

Banacos, P. C., and D. M. Schultz, 2005: The use of moisture flux convergence in forecasting convective initiation: Historical and operational perspectives. *Wea. Forecasting*, **20**, 351–366, https://doi.org/10.1175/WAF858.1.

Baranowski, D. B., M. K. Flatau, P. J. Flatau, and A. J. Matthews, 2016: Phase locking between atmospheric convectively coupled equatorial Kelvin waves and the diurnal cycle of precipitation over the Maritime Continent. *Geophys. Res. Lett.*, **43**, 8269–8276, https://doi.org/10.1002/2016GL069602.

Biasutti, M., S. E. Yuter, C. D. Burleyson, and A. H. Sobel, 2012: Very high resolution rainfall patterns measured by TRMM precipitation radar: Seasonal and diurnal cycles. *Climate Dyn.*, **39**, 239–258, https://doi.org/10.1007/s00382-011-1146-6.

Birch, C. E., S. Webster, S. C. Peatman, D. J. Parker, A. J. Matthews, Y. Li, and M. E. E. Hassim, 2016: Scale interactions between the MJO and the western Maritime Continent. *J. Climate*, **29**, 2471–2492, https://doi.org/10.1175/JCLI-D-15-0557.1.

Cao, X., T. Li, M. Peng, W. Chen, and G. Chen, 2014: Effects of monsoon trough intraseasonal oscillation on tropical cyclogenesis over the western North Pacific. *J. Atmos. Sci.*, **71**, 4639–4660, https://doi.org/10.1175/JAS-D-13-0407.1.

Chang, C. P., Z. Wang, J. Ju, and T. Li, 2004: On the relationship between western Maritime Continent monsoon rainfall and ENSO during northern winter. *J. Climate*, **17**, 665–672, https://doi.org/10.1175/1520-0442(2004)017<0665:OTRBWM>2.0.CO;2.

——, ——, J. McBride, and C. Liu, 2005: Annual cycle of Southeast Asia–Maritime Continent rainfall and the asymmetric monsoon transition. *J. Climate*, **18**, 287–301, https://doi.org/10.1175/JCLI-3257.1.

Chen, L., T. Li, and Y. Yu, 2015: Causes of strengthening and weakening of ENSO amplitude under global warming in four CMIP5 models. *J. Climate*, **28**, 3250–3274, https://doi.org/10.1175/JCLI-D-14-00439.1.

Chen, S. S., and R. A. Houze Jr., 1997: Diurnal variation and lifecycle of deep convective systems over the tropical Pacific warm pool. *Quart. J. Roy. Meteor. Soc.*, **123**, 357–388, https://doi.org/10.1002/qj.49712353806.

Dai, A., 2001: Global precipitation and thunderstorm frequencies. Part II: Diurnal variations. *J. Climate*, **14**, 1112–1128, https://doi.org/10.1175/1520-0442(2001)014<1112:GPATFP>2.0.CO;2.

Deser, C., and C. A. Smith, 1998: Diurnal and semidiurnal variations of the surface wind field over the tropical Pacific Ocean. *J. Climate*, **11**, 1730–1748, https://doi.org/10.1175/1520-0442(1998)011<1730:DASVOT>2.0.CO;2.

Du, Y., and R. Rotunno, 2015: Thermally driven diurnally periodic wind signals off the east coast of China. *J. Atmos. Sci.*, **72**, 2806–2821, https://doi.org/10.1175/JAS-D-14-0339.1.

——, and ——, 2018: Diurnal cycle of rainfall and winds near the south coast of China. *J. Atmos. Sci.*, **75**, 2065–2082, https://doi.org/10.1175/JAS-D-17-0397.1.

Frenkel, Y., B. Khouider, and A. J. Majda, 2011: Simple multicloud models for the diurnal cycle of tropical precipitation. Part I: Formulation and the case of the tropical oceans. *J. Atmos. Sci.*, **68**, 2169–2190, https://doi.org/10.1175/2011JAS3568.1.

Gray, W. M., and R. W. Jacobson Jr., 1977: Diurnal variation of deep cumulus convection. *Mon. Wea. Rev.*, **105**, 1171–1188, https://doi.org/10.1175/1520-0493(1977)105<1171:DVODCC>2.0.CO;2.

Haylock, M., and J. McBride, 2001: Spatial coherence and predictability of Indonesian wet season rainfall. *J. Climate*, **14**, 3882–3887, https://doi.org/10.1175/1520-0442(2001)014<3882:SCAPOI>2.0.CO;2.

Hendon, H. H., 2003: Indonesian rainfall variability: Impacts of ENSO and local air–sea interaction. *J. Climate*, **16**, 1775–1790, https://doi.org/10.1175/1520-0442(2003)016<1775:IRVIOE>2.0.CO;2.

——, and K. Woodberry, 1993: The diurnal cycle of tropical convection. *J. Geophys. Res.*, **98**, 16 623–16 637, https://doi.org/10.1029/93JD00525.

Hsu, P.-C., T. Li, and C.-H. Tsou, 2011: Interactions between boreal summer intraseasonal oscillations and synoptic-scale disturbances over the western North Pacific. Part I: Energetics diagnosis. *J. Climate*, **24**, 927–941, https://doi.org/10.1175/2010JCLI3833.1.

Huffman, G. J., and Coauthors, 2007: The TRMM Multisatellite Precipitation Analysis (TMPA): Quasi-global, multiyear, combined-sensor precipitation estimates at fine scales. *J. Hydrometeor.*, **8**, 38–55, https://doi.org/10.1175/JHM560.1.

Hung, C., and C. Sui, 2018: A diagnostic study of the evolution of the MJO from Indian Ocean to Maritime Continent: Wave dynamics versus advective moistening processes. *J. Climate*, **31**, 4095–4115, https://doi.org/10.1175/JCLI-D-17-0139.1.

Ichikawa, H., and T. Yasunari, 2006: Time and space characteristics of diurnal rainfall over Borneo and surrounding oceans as observed by TRMM-PR. *J. Climate*, **19**, 1238–1260, https://doi.org/10.1175/JCLI3714.1.

——, and ——, 2008: Intraseasonal variability in diurnal rainfall over New Guinea and the surrounding oceans during austral summer. *J. Climate*, **21**, 2852–2868, https://doi.org/10.1175/2007JCLI1784.1.

Janowiak, J. E., P. A. Arkin, and M. Morrissey, 1994: An examination of the diurnal cycle in oceanic tropical rainfall using satellite and in situ data. *Mon. Wea. Rev.*, **122**, 2296–2311, https://doi.org/10.1175/1520-0493(1994)122<2296:AEOTDC>2.0.CO;2.

Jiang, L., and T. Li, 2018: Why rainfall response to El Niño over Maritime Continent is weaker and non-uniform in boreal winter than in boreal summer. *Climate Dyn.*, **51**, 1465–1483, https://doi.org/10.1007/s00382-017-3965-6.

Kikuchi, K., and B. Wang, 2008: Diurnal precipitation regimes in the global tropics. *J. Climate*, **21**, 2680–2696, https://doi.org/10.1175/2007JCLI2051.1.

Kraus, E. B., 1963: The diurnal precipitation change over the sea. *J. Atmos. Sci.*, **20**, 551–556, https://doi.org/10.1175/1520-0469(1963)020<0551:TDPCOT>2.0.CO;2.

Kubota, H., and T. Nitta, 2001: Diurnal variations of tropical convection observed during the TOGA-COARE. *J. Meteor. Soc. Japan*, **79**, 815–830, https://doi.org/10.2151/jmsj.79.815.

Lorenz, E. N., 1956: *Empirical Orthogonal Functions and Statistical Weather Prediction*. Statistical Forecasting Project Scientific Rep. 1, Massachusetts Institute of Technology, 49 pp.

Love, B. S., A. J. Matthews, and G. M. S. Lister, 2011: The diurnal cycle of precipitation over the Maritime Continent in a high-resolution atmospheric model. *Quart. J. Roy. Meteor. Soc.*, **137**, 934–947, https://doi.org/10.1002/qj.809.

Lu, J., T. Li, and L. Wang, 2019: Precipitation diurnal cycle over the Maritime Continent modulated by the MJO. *Climate Dyn.*, **53**, 6489–6501, https://doi.org/10.1007/s00382-019-04941-8.

Mori, S., and Coauthors, 2004: Diurnal land–sea rainfall peak migration over Sumatera Island, Indonesian Maritime Continent, observed by TRMM satellite and intensive rawinsonde soundings. *Mon. Wea. Rev.*, **132**, 2021–2039, https://doi.org/10.1175/1520-0493(2004)132<2021:DLRPMO>2.0.CO;2.

Neale, R. B., and J. M. Slingo, 2003: The Maritime Continent and its role in the global climate: A GCM study. *J. Climate*, **16**, 834–848, https://doi.org/10.1175/1520-0442(2003)016<0834:TMCAIR>2.0.CO;2.

Negri, A. J., T. L. Bell, and L. Xu, 2002: Sampling of the diurnal cycle of precipitation using TRMM. *J. Atmos. Oceanic Technol.*, **19**, 1333–1344, https://doi.org/10.1175/1520-0426(2002)019<1333:SOTDCO>2.0.CO;2.

Peatman, S. C., A. J. Matthews, and D. P. Stevens, 2014: Propagation of the Madden–Julian Oscillation through the Maritime Continent and scale interaction with the diurnal cycle of precipitation. *Quart. J. Roy. Meteor. Soc.*, **140**, 814–825, https://doi.org/10.1002/qj.2161.

——, ——, and ——, 2015: Propagation of the Madden–Julian Oscillation and scale interaction with the diurnal cycle in a high-resolution GCM. *Climate Dyn.*, **45**, 2901–2918, https://doi.org/10.1007/s00382-015-2513-5.

Qian, J. H., 2008: Why precipitation is mostly concentrated over islands in the Maritime Continent. *J. Atmos. Sci.*, **65**, 1428–1441, https://doi.org/10.1175/2007JAS2422.1.

——, A. W. Robertson, and V. Moron, 2010: Interactions among ENSO, the monsoon, and diurnal cycle in rainfall variability over Java, Indonesia. *J. Atmos. Sci.*, **67**, 3509–3524, https://doi.org/10.1175/2010JAS3348.1.

Ramage, C. S., 1968: Role of a tropical "Maritime Continent" in the atmospheric circulation. *Mon. Wea. Rev.*, **96**, 365–370, https://doi.org/10.1175/1520-0493(1968)096<0365:ROATMC>2.0.CO;2.

——, 1971: *Monsoon Meteorology*. Academic Press, 296 pp.

Randall, D. A., Harshvardhan, and D. A. Dazlich, 1991: Diurnal variability of the hydrologic cycle in a general circulation model. *J. Atmos. Sci.*, **48**, 40–62, https://doi.org/10.1175/1520-0469(1991)048<0040:DVOTHC>2.0.CO;2.

Rauniyar, S. P., and K. J. E. Walsh, 2011: Scale interaction of the diurnal cycle of rainfall over the Maritime Continent and Australia: Influence of the MJO. *J. Climate*, **24**, 325–348, https://doi.org/10.1175/2010JCLI3673.1.

——, and ——, 2013: Influence of ENSO on the diurnal cycle of rainfall over the Maritime Continent and Australia. *J. Climate*, **26**, 1304–1321, https://doi.org/10.1175/JCLI-D-12-00124.1.

Rienecker, M., and Coauthors, 2011: MERRA: NASA's Modern-Era Retrospective Analysis for Research and Applications. *J. Climate*, **24**, 3624–3648, https://doi.org/10.1175/JCLI-D-11-00015.1.

Sakaeda, N., G. Kiladis, and J. Dias, 2017: The diurnal cycle of tropical cloudiness and rainfall associated with the Madden–Julian oscillation. *J. Climate*, **30**, 3999–4020, https://doi.org/10.1175/JCLI-D-16-0788.1.

——, S. W. Powell, J. Dias, and G. N. Kiladis, 2018: The diurnal variability of precipitating cloud populations during DYNAMO. *J. Atmos. Sci.*, **75**, 1307–1326, https://doi.org/10.1175/JAS-D-17-0312.1.

Sakurai, N., and Coauthors, 2005: Diurnal cycle of cloud system migration over Sumatera Island. *J. Meteor. Soc. Japan*, **83**, 835–850, https://doi.org/10.2151/jmsj.83.835.

Simpson, J., T. D. Keenan, B. Ferrier, R. H. Simpson, and G. J. Holland, 1993: Cumulus mergers in the Maritime Continent region. *Meteor. Atmos. Phys.*, **51**, 73–99, https://doi.org/10.1007/BF01080881.

Smith, W. H. F., and D. T. Sandwell, 1997: Global seafloor topography from satellite altimetry and ship depth soundings. *Science*, **277**, 1956–1962, https://doi.org/10.1126/science.277.5334.1956.

Sui, C.-H., K.-M. Lau, Y. N. Takayabu, and D. A. Short, 1997: Diurnal variations in tropical oceanic cumulus convection during TOGA COARE. *J. Atmos. Sci.*, **54**, 639–655, https://doi.org/10.1175/1520-0469(1997)054<0639:DVITOC>2.0.CO;2.

Teo, C., T. Koh, J. C. Lo, and B. C. Bhatt, 2011: Principal component analysis of observed and modeled diurnal rainfall in the Maritime Continent. *J. Climate*, **24**, 4662–4675, https://doi.org/10.1175/2011JCLI4047.1.

Tian, B., B. J. Soden, and X. Wu, 2004: Diurnal cycle of convection, clouds, and water vapor in the tropical upper troposphere: Satellites versus a general circulation model. *J. Geophys. Res.*, **109**, D10101, https://doi.org/10.1029/2003JD004117.

Uppala, S. M., D. Dee, S. Kobayashi, P. Berrisford, and A. Simmons, 2008: Towards a climate data assimilation system: Status update of ERA-Interim. *ECMWF Newsletter*, No. 115, ECMWF, Reading, United Kingdom, 12–18, https://www.ecmwf.int/publications/newsletters/pdf/115_rev.pdf.

Vincent, C. L., T. P. Lane, and M. C. Wheeler, 2016: A local index of Maritime Continent intraseasonal variability based on rain rates over the land and sea. *Geophys. Res. Lett.*, **43**, 9306–9314, https://doi.org/10.1002/2016GL069987.

Wang, B., and X.-S. Xie, 1996: Low-frequency equatorial waves in vertically sheared zonal flow. Part I: Stable waves. *J. Atmos. Sci.*, **53**, 449–467, https://doi.org/10.1175/1520-0469(1996)053<0449:LFEWIV>2.0.CO;2.

——, H.-J. Kim, K. Kikuchi, and A. Kitoh, 2011: Diagnostic metrics for evaluation of annual and diurnal cycles. *Climate Dyn.*, **37**, 941–955, https://doi.org/10.1007/s00382-010-0877-0.

Wang, L., T. Li, E. Maloney, and B. Wang, 2017: Fundamental causes of propagating and nonpropagating MJOs in MJOTF/GASS models. *J. Climate*, **30**, 3743–3769, https://doi.org/10.1175/JCLI-D-16-0765.1.

——, ——, and L. Chen, 2019: Modulation of the Madden–Julian Oscillation on the energetics of wintertime synoptic-scale disturbances. *Climate Dyn.*, **52**, 4861–4871, https://doi.org/10.1007/s00382-018-4447-1.

Worku, L. Y., A. Mekonnen, and C. J. Schreck, 2019: Diurnal cycle of rainfall and convection over the Maritime Continent using TRMM and ISCCP. *Int. J. Climatol.*, **39**, 5191–5200, https://doi.org/10.1002/joc.6121.

Wu, P., M. Hara, J. Hamada, M. D. Yamanaka, and F. Kimura, 2009: Why a large amount of rain falls over the sea in the vicinity of western Sumatra Island during nighttime. *J. Appl. Meteor. Climatol.*, **48**, 1345–1361, https://doi.org/10.1175/2009JAMC2052.1.

Yanase, A., K. Yasunaga, and H. Masunaga, 2017: Relationship between the direction of diurnal rainfall migration and the ambient wind over the southern Sumatra Island. *Earth Space Sci.*, **4**, 117–127, https://doi.org/10.1002/2016EA000181.

Yang, G.-Y., and J. Slingo, 2001: The diurnal cycle in the tropics. *Mon. Wea. Rev.*, **129**, 784–801, https://doi.org/10.1175/1520-0493(2001)129<0784:TDCITT>2.0.CO;2.

Yang, S., and E. A. Smith, 2006: Mechanisms for diurnal variability of global tropical rainfall observed from TRMM. *J. Climate*, **19**, 5190–5226, https://doi.org/10.1175/JCLI3883.1.

Zhou, L., and Y. Wang, 2006: Tropical Rainfall Measuring Mission observation and regional model study of precipitation diurnal cycle in the New Guinean region. *J. Geophys. Res.*, **111**, D17104, https://doi.org/10.1029/2006JD007243.